

# Multiscale AM-FM Methods for Diabetic Retinopathy Lesion Detection

Carla Agurto\*, *Student Member, IEEE*, Victor Murray, *Member, IEEE*, Eduardo Barriga, *Member, IEEE*, Sergio Murillo, Marios Pattichis, *Senior Member, IEEE*, Herbert Davis, Stephen Russell, Michael Abràmoff, *Member, IEEE*, and Peter Soliz, *Member, IEEE*

**Abstract**—In this paper, we propose the use of multiscale amplitude-modulation-frequency-modulation (AM-FM) methods for discriminating between normal and pathological retinal images. The method presented in this paper is tested using standard images from the early treatment diabetic retinopathy study. We use 120 regions of  $40 \times 40$  pixels containing four types of lesions commonly associated with diabetic retinopathy (DR) and two types of normal retinal regions that were manually selected by a trained analyst. The region types included microaneurysms, exudates, neovascularization on the retina, hemorrhages, normal retinal background, and normal vessels patterns. The cumulative distribution functions of the instantaneous amplitude, the instantaneous frequency magnitude, and the relative instantaneous frequency angle from multiple scales are used as texture feature vectors. We use distance metrics between the extracted feature vectors to measure interstructure similarity. Our results demonstrate a statistical differentiation of normal retinal structures and pathological lesions based on AM-FM features. We further demonstrate our AM-FM methodology by applying it to classification of retinal images from the MESSIDOR database. Overall, the proposed methodology shows significant capability for use in automatic DR screening.

**Index Terms**—Automatic screening, diabetic retinopathy (DR), multiscale amplitude-modulation-frequency-modulation (AM-FM) methods.

## I. INTRODUCTION

**M**OST methods developed for the detection of diabetic retinopathy (DR) require the development of a specific segmentation technique for each of the number of abnormalities found on the retina, such as microaneurysms (MAs), exudates, etc. [1]–[4]. Here we present a new texture-based modeling technique that avoids the difficulties of explicit feature segmentation techniques used by some current methodologies in

detection of DR in retinal images. This approach utilizes amplitude-modulation-frequency-modulation (AM-FM) methods for the characterization of retinal structures [5].

To apply feature segmentation, various researchers find it necessary to train the algorithm on reference images. This requires manually annotated individual lesions. Providing these is a tedious and time-consuming activity, which has hampered the application of the algorithms to digital retinal images with varying image formats, e.g., compressed images, images of different sizes, etc. Generalized texture modeling techniques that avoid manual segmentation would greatly enhance progress toward an automated screening of retinal images.

Another common problem when applying image processing methods to retinal images is the need for correction of uneven illumination. The first step in the analysis of retinal images has commonly been to process the images to remove lighting artifacts, which enhances detection of lesions. Osareh *et al.* [6], [7] used color normalization and local contrast enhancement as an initial step for detecting exudates. Spencer *et al.* [8], Frame *et al.* [9], and Niemeijer *et al.* [10] removed the slow gradients in the background of the green channel of each image resulting in a shade-corrected image.

Other approaches are focused on the development of preprocessing steps for the detection and subsequent removal of normal anatomical “background” structures in the image. Fleming *et al.* [11] applied a  $3 \times 3$  pixel median filter to reduce this variation. They convolved the retinal image with a Gaussian filter, and then normalized the image for the detection of exudates. Other methods segment and remove retinal vessels that simulate red lesions [12]–[14]. Our method is like the approach described by Niemeijer *et al.* [15], which does not require any preprocessing. In our method, the green channel of the image is the input for applying the feature extraction technique.

Much of the published literature on retinal lesion detection has focused either on the detection of red lesions such as MAs and hemorrhages or detection of bright lesions such as exudates and cotton wool spots. Niemeijer *et al.* [11], Larsen *et al.* [1], and Sander *et al.* [4] described methods for detecting red lesions. Similarly, Streeter *et al.* [16] and Jelinek *et al.* [17] developed systems for detecting MAs only. Niemeijer *et al.* [15] also proposed an automated method for the differentiation and detection of exudates, cotton wool spots, which are characteristics of DR, and age-related macular degeneration, respectively. Similarly, Sopharak *et al.* [18] and Osareh *et al.* [5] developed methods for the detection of exudates.

The extraction of features in the diagnosis of a retinal image is commonly the basis for an automatic classification system. The

Manuscript received September 08, 2009; revised November 09, 2009; accepted November 09, 2009. Current version published February 03, 2010. This work was supported in part by the National Eye Institute under Grant EY018280. Asterisk indicates corresponding author.

\*C. Agurto is with the Department of Electrical and Computer Engineering, University of New Mexico, Albuquerque, NM 87109 USA (e-mail: capaagri@unm.edu).

V. Murray, M. S. Pattichis, and S. Murillo are with the Department of Electrical and Computer Engineering, University of New Mexico, Albuquerque, NM 87109 USA (e-mail: vmurray@ieee.org; pattichis@ece.unm.edu; smurillo@ece.unm.edu).

S. Russell and M. D. Abràmoff are with the Department of Ophthalmology and Visual Sciences, University of Iowa Hospitals and Clinics, Iowa City, IA 52242 USA (e-mail: michael-abramoff@uiowa.edu; steve-russell@uiowa.edu).

E. S. Barriga, H. Davis, and P. Soliz are with VisionQuest Biomedical, Albuquerque, NM 87106 USA (e-mail: sbarriga@visionquest-bio.com; bert@visionquest-bio.com; psoliz@visionquest-bio.com).

Digital Object Identifier 10.1109/TMI.2009.2037146

most popular methods for feature extraction are morphology in the detection of exudates [18], [19], Gabor filters in the detection and differentiation of bright lesions [15], and the classification of retinal images [20], wavelet transforms in the detection of MAs by Quellec *et al.* [21], [22], and Match filters for vessel extraction [23], [24].

The main contribution of our research is the rigorous characterization of normal and pathological retinal structures based on their instantaneous amplitude (IA) and instantaneous frequency (IF) characteristics, and a high area under the receiver operating characteristic (ROC) for the detection of DR in retinal images. This paper analyzes six different types of retinal structures in the retina, and discusses how AM-FM texture features can be used for differentiating among them.

The organization of this paper is as follows. Section II describes the methodology used for the characterization of the structures in the retina. The AM-FM methodology is explained using early treatment diabetic retinopathy study (ETDRS) images. The results are shown and explained in Section III. Results are based on the classification of 400 images from the Messidor database. Finally, the discussion is presented in Section IV.

## II. METHODS

### A. Database

Images were selected from the online ETDRS database [25]. Working images are uncompressed telephone influence factor (TIF) format with a size of  $1000 \times 1060$  pixels. The ETDRS standard photographs contain 15 stereo pair images that are used to train graders on DR. From these images, 120 regions of  $40 \times 40$  pixels containing retinal structures of interest were selected for this study. These regions were grouped into six categories of 20 regions per structure: MAs, hemorrhages, exudates, neovascularization (NV), retinal background (RB), and vessels. Fig. 1(a) shows one of the standard ETDRS images used in this paper with abnormal retinal structures delimited by boxes. Fig. 1(b) shows samples of the structures aforementioned on regions of interest (ROI) of  $40 \times 40$  pixels in size.

### B. AM-FM Decompositions

An image can be approximated by a sum of AM-FM components given by

$$I(x, y) \approx \sum_{n=1}^M a_n(x, y) \cos \varphi_n(x, y) \quad (1)$$

where  $M$  is the number of AM-FM components,  $a_n(x, y)$  denote IA functions, and  $\varphi_n(x, y)$  denote the instantaneous phase functions [26]. We refer to [27] for further details on the use of AM-FM decomposition. Here, our focus will be on the extraction of AM-FM texture features.

First, we extract AM-FM components from each image scale, as outlined in Section II-C. For each AM-FM component, the IF is defined in terms of the gradient of the phase  $\varphi_n$  as

$$\nabla \varphi_n(x, y) = \left( \frac{\partial \varphi_n(x, y)}{\partial x}, \frac{\partial \varphi_n(x, y)}{\partial y} \right). \quad (2)$$

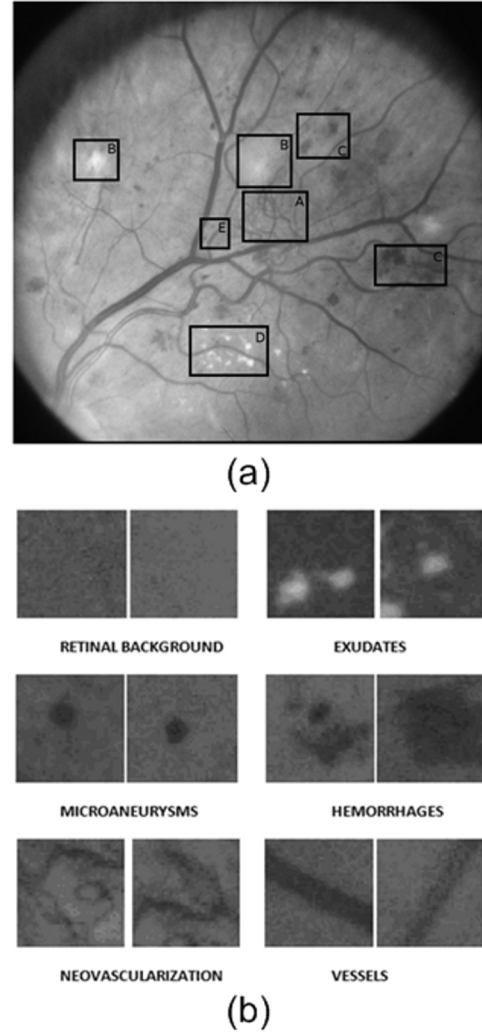


Fig. 1. (a) Image from the ETDRS standard database. Lesions encased in the boxes are examples of: (1) NV, (2) cottonwool spots, (3) hemorrhages, (4) exudates, and (5) MAs. (b) Examples of retinal structures on ROIs of  $40 \times 40$  pixels.

In terms of extracting textural features from each component, we are interested in using the IF and the IA. Conceptually, the IF measures local frequency content. When expressed in terms of cycles per millimeter, the IF magnitude is independent of any image rotations or retinal imaging hardware characteristics, since it reflects an actual physical measurement of local image texture, extracted from each image scale. Furthermore, the IF magnitude is a measurement of the geometry of the texture, with a strong degree of independence from contrast and nonuniform illumination variations.

We are also interested in working with an invariant IF angle feature. To this end, instead of using the actual IF angle, we use relative angles. Here, relative angles are estimated locally as deviations from the dominant neighborhood angle. Thus, directional structures, such as blood vessels will produce a relative angle distribution concentrated around zero. We constraint the relative angle to range from  $-\pi/2$  to  $\pi/2$ . Thus, a sign ambiguity occurs from the fact that  $\cos \varphi(x, y)$  represents the same image as  $\cos[-\varphi(x, y)]$ .

TABLE I  
BANDPASS FILTERS ASSOCIATED WITH MULTIPLE IMAGE SCALES

Frequency Scale Band	Filters	Instantaneous Wavelength (period) Range in pixels	Range in mm
Low Pass Filter (LPF)	1	22.6 to $\infty$	0.226 to $\infty$
Very Low Frequencies (VL)	20-25	11.3 to 32	0.113 to 0.32
Low Frequencies (L)	14-19	5.7 to 16	0.057 to 0.16
Medium Frequencies (M)	8-13	2.8 to 8	0.028 to 0.08
High Frequencies (H)	2-7	1.4 to 4	0.014 to 0.04

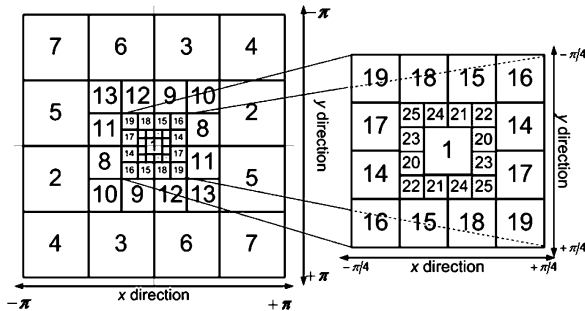


Fig. 2. Filter bank for multiscale AM-FM decomposition. The discrete spectrum is decomposed using 25 bandpass filters for each scale (see Table I).

Local image intensity variations, including edges, are reflected in the IA. As we shall discuss next, large spatial scale variations will be reflected in the low-frequency scales.

### C. Frequency Scales and Filter Banks

AM-FM components are extracted from different image scales. We consider the use of 25 bandpass channel filters associated with four frequency scales and nine possible combinations of scales (CoS) (see Fig. 2). We estimate a single AM-FM component over each combination of scales using dominant component analysis (DCA) [5], [27].

At lower frequency scales, the magnitude values of the  $|IF|$  are small and the extracted AM-FM features reflect slowly varying image texture. For example, the most appropriate scale for blood vessels is the one that captures frequencies with a period that is proportional to their width. On the other hand, the fine details within individual lesions, such as the small vessels in neovascular structures, are captured by the higher frequency scales. To analyze the image at different scales, we use a multiscale channel decomposition outlined in Fig. 2.

The use of different scales also considers the size variability among structures such as MAs, exudates, hemorrhages, etc. A predominant characteristic of patients with DR is that the lesion sizes will vary. Dark lesions such as MAs, or bright lesions such as exudates, may be present in an image as structures with areas on the order of a few pixels. In the images that were analyzed for this study, the MAs' and exudates' diameters are on the order of 8 pixels, which represent a size 0.04 mm. Hemorrhages and cotton wool spots diameters are on the order of 25 pixels, representing a size of 0.12 mm. Multiple scales are used to capture these features of different sizes. The different filters (within any given scale) also consider the orientation of the feature being encoded.

TABLE II  
COMBINATIONS OF SCALES

Combination Number	Filters	Frequency Bands	Range in cycles/mm
1	8:25	M + L + VL	0.028 to 0.32
2	1	LPF	0.226 to $\infty$
3	20:25	VL	0.113 to 0.32
4	14:19	L	0.057 to 0.16
5	8:13	M	0.028 to 0.08
6	14:25	L + VL	0.057 to 0.32
7	8:19	M + L	0.028 to 0.16
8	2:7	H	0.014 to 0.04
9	2:13	H+M	0.014 to 0.08

Table I relates the number of pixels and the frequency ranges of each bandpass filter shown in Fig. 2. The CoS were grouped in such a way that contiguous frequency bands were covered. In this way, structures that only appear in a specific frequency range or appear between two or three contiguous bands can also be described. For this reason, the nine CoS, presented in Table II, were grouped to encode the features for different structures.

Twenty-seven AM-FM histogram estimates were computed corresponding to the three AM-FM features IA,  $|IF|$ , and relative angle, for each of the nine CoS. The bandpass filters were implemented using an equiripple dyadic finite-impulse response (FIR) filters design, and have a passband and a stopband ripple of 0.001 and 0.0005 dB, respectively [5]. Robust AM-FM demodulation was applied over each bandpass filter [5], [28]. The AM-FM demodulation algorithm has been shown to yield significantly improved AM-FM estimates via the use of the equiripple filter bank and a variable-spacing linear-phase approximation [5], [28]. Then, at each pixel, for each combination of scales, we use DCA to select the AM-FM features from the bandpass filter that gave the maximum IA estimate. Figs. 3–5 shows some examples of the AM-FM estimates obtained after applying to three of the images in the ETDRS dataset.

### D. Encoding of Structures Using AM-FM

To characterize the retinal structures, the cumulative distribution functions (CDFs) of the IA,  $|IF|$ , and the relative angle are used. Since the range of values of each estimate varies according to the CoS used, the histograms (or pdf) are computed from the global minimum value to the global maximum value. For example, for the IA using CoS 4 (low frequencies), the histograms were computed in the range of [0 72] pixels because this is the grayscale range for the IA in which the low frequencies are supported.

A region with small pixel intensity variation will also be characterized by low IA values in the higher frequency scales.

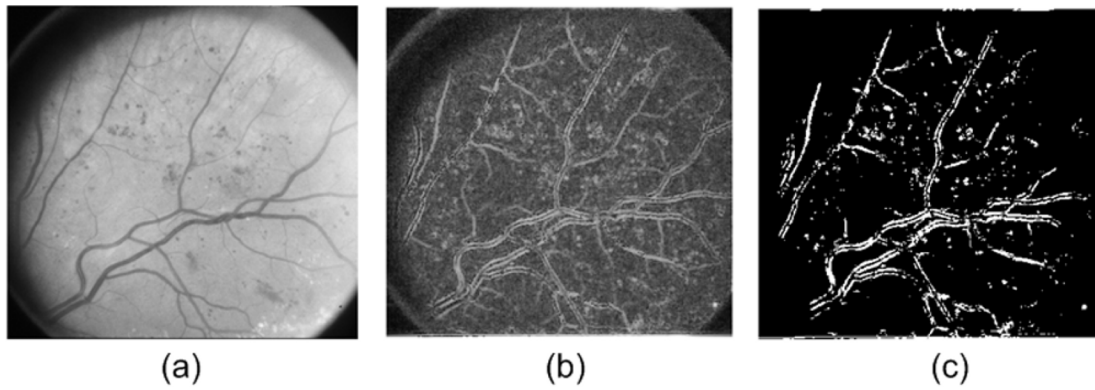


Fig. 3. (a) Original image from ETDRS. (b) IA using medium, low, and very low frequencies. (c) Thresholded image of (b).

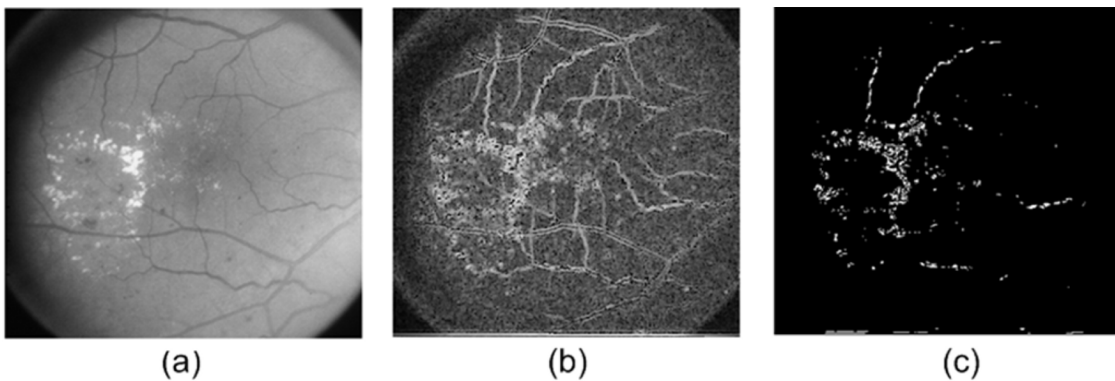


Fig. 4. (a) Original image from ETDRS. (b) IA using low frequencies. (c) Thresholded image of (b).

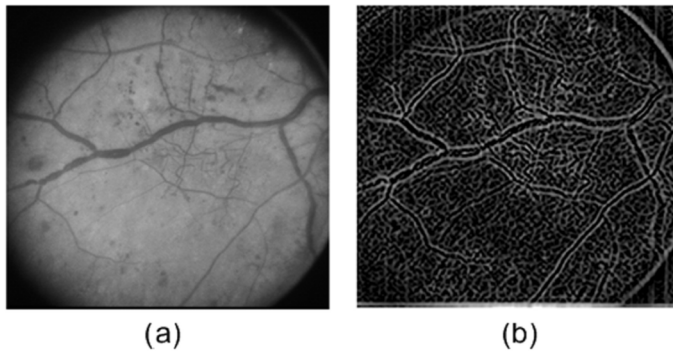


Fig. 5. (a) Original image from ETDRS. (b) IF magnitude using low-pass filter.

This is due to the fact that low-intensity variation regions will also contain weak-frequency components. Furthermore, darker regions will also be characterized by low IA values in the lower frequency scales. This is due to the linearity of the AM-FM decomposition. Low-amplitude image regions will mostly need low-amplitude AM-FM components. For example, RB [see Fig. 1(b)] analyzed in the whole frequency spectrum will have roughly constant, low IA values. In general, for any given scale, low IA values will reflect the fact that frequency components from that particular scale are not contained in the image. Thus, since there are no high IA values to account for, the CDF of this kind of structure is expected to rise rapidly for low IA values. On the other hand, if a region contains structures with

significant edges and intensity variations such as vessels, MAs, NV, or exudates, we expect that the rate of rise (pdf) of their CDFs will be slower due to the presence of both low and high IA components.

#### *E. Defining Retinal Characteristics of AM-FM Feature Vectors*

In this section, we describe how the AM-FM estimates encode structures and how this encoding can be related to the creation of relevant feature vectors for the detection of the analyzed lesions.

The IF magnitude ( $|IF|$ ) is insensitive to the direction of image intensity variations. Furthermore, the IF magnitude is a function of the local geometry as opposed to the slowly varying brightness variations captured in the IA. Thus, a single dark round structure in a lighter background will have similar  $|IF|$  distribution as a single bright round structure of the same size in darker region. This is roughly the case for exudates (bright lesions) and MAs (dark lesions) when they have similar areas.  $|IF|$  estimates can be used for differentiating between two regions where one has a single vessel (as in a normal retinal vessel) and a second region that has multiple narrow vessels (as in NV). Even though both regions may have information in the same frequency ranges, the counts on the histogram of the latter region will be greater. The larger histogram counts reflect the fact that a larger number of pixels exhibit these frequency components. The histogram for a region with NV will have higher kurtosis (a more pronounced peak) than a region containing just one vessel.

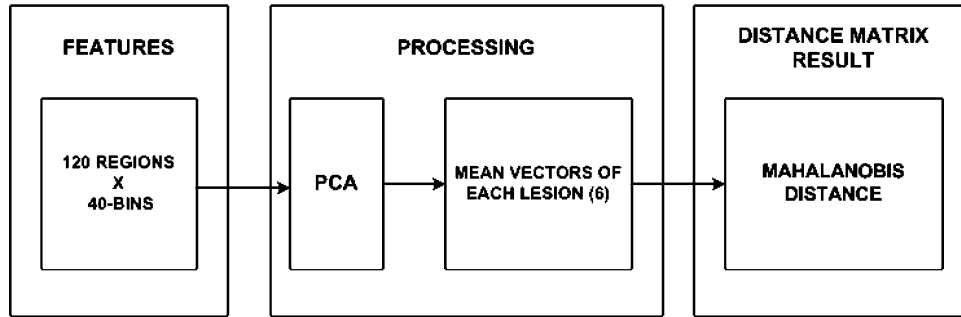


Fig. 6. Procedure to find the Mahalanobis distance between lesions for each estimate and each CoS. First the features for the regions are extracted per estimate (IA, |IF|, and relative angle). Then a reduction of dimensionality method (PCA) is applied for each feature estimate of the regions. After that, the mean of 20 regions corresponding to a specific lesion is found. Using the information of the six means, the Mahalanobis distance is found for each estimate. This process is repeated for each CoS given as a result 27 different distances between lesions.

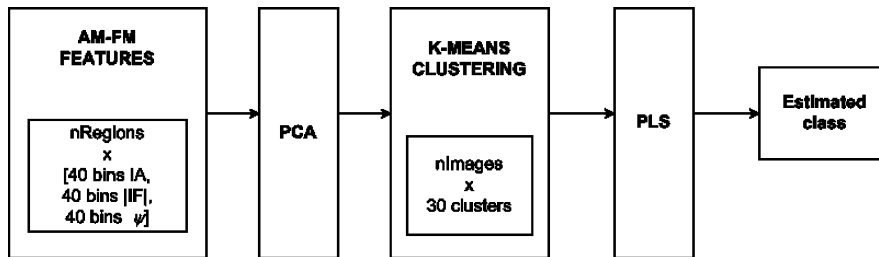


Fig. 7. Procedure to classify retinal images. First, the features are extracted using AM-FM. Then a reduction of dimensionality method (PCA) is applied for each CoS. After that, an unsupervised method called k-means clustering is applied in order to reduce the dimensionality. Finally, the PLS is applied to obtain the estimated class for each image.

We also analyze image regions in terms of the relative IF angle. First, we note that image structures without any dominant orientation will have a relatively flat histogram (regardless of what is chosen as the dominant orientation). This kind of feature should be observed on structures such as MAs and exudates. Conversely, an area with a single vessel in a region has a unique angle of inclination. In this case, the (nonrelative) IF angle estimate is expected to be highly peaked at the inclination angle, assigning much smaller count values to angles that are further away from the angle of inclination. Then, as discussed earlier, the relative angle histograms will have their peak at zero. One last case includes structures within a region that have several elements with different orientations, such as NV. The histograms for these regions would include several well-defined peaks at different angles. Thus, this feature can be differentiated from the other two well-defined distributions described before.

#### F. Classification

In order to demonstrate that the methodology presented in this paper can distinguish between the structures in the retina, two types of classification were performed. The first one is focused on the classification of small regions containing structures and the second one is focused on the greater problem of classification of retinal images as a DR or non-DR. For the first classification test, a well-known statistical metric, the Mahalanobis distance, is computed. Fig. 6 shows the procedure to calculate the distance between the lesions for each of the nine CoS. First, the CDF is extracted for each of the three estimates in the 120

regions. After that, the dimensionality of the feature vectors is reduced using principal component analysis (PCA), where the principal component projections are chosen so as to account for 95% of the variance. This procedure is applied for each of the nine CoS. In this way, the combinations and the estimates that produce the greatest distance between lesions can be found. It is important to mention that in order to normalize the calculation of the distance between lesions, the reduced matrix is adjusted to have standard deviation 1 and the distances of the lesions with respect to a specific lesion are calculated between mean vectors.

In our second experiment, using a cross-validation approach, we classified retinas from healthy subjects and subjects that had different levels of DR. To test the significance of the AM-FM processing as a methodology for the extraction of features, 376 images of the MESSIDOR database [29] were selected. These images are classified by ophthalmologists in four levels, where Risk 0 correspond to non-DR images, Risk 1 to mild DR, Risk 2 to moderate DR, and Risk 3 corresponds to an advanced stage of DR. Table III shows the distribution of the dataset used for the experiment. The retinal image was divided in regions of  $100 \times 100$  pixels. We excluded the optic disc for our analysis. A total of 100 regions were obtained for each retinal image. The procedure to extract the features and reduce their dimensionality is the same as our first experiment. After the features are extracted, we used *k*-means clustering (an unsupervised classification method) to cluster the information in 30 groups, so a feature vector for each image can be obtained. This vector represents the number of regions in each of the 30 clusters for each image. For testing purposes, the centroids are stored for each

TABLE III  
DATABASE INFORMATION

DR RISK	Number of Images	Number of MA	Number of Hemorrhages	Neovascularization
RISK 0	140	0	0	0
RISK 1	28	[ 1, 5]	0	0
RISK 2	68	<5,15>	[0, 5]	0
RISK 3	140	[15, ∞>	[5, ∞>	1

Any of the three conditions for the number of hemorrhages or the number of microaneurysms should be held to consider the image as RISK 2 and Risk 3. Some of the retinal images of Risk2 present exudates and some of the retinal images of Risk3 present exudates, and neovascularization. Macular edema was graded separately as either none, >1DD from fovea or <1DD from fovea (clinically significant Macular edema, CSME).

TABLE IV  
MAXIMUM DISTANCE MATRIX BETWEEN LESIONS

Retinal Structures	RB	EX	MA	HE	NV
EX	6.87	0	-	-	-
MA	3.48	3.97	0	-	-
HE	4.72	4.89	4.71	0	-
NV	8.18	4.59	2.92	2.65	0
VE	6.14	3.31	2.83	3.51	3.35

RB: Retinal Background, EX: Exudate,  
MA: Microaneurysm, HE: Hemorrhage  
NV: Neovascularization, VE: Vessel

cluster. Finally, a linear regression method, partial least square (PLS), was applied to derive classes and the loading matrix, and the coefficient factors were stored for the testing stage.

### III. RESULTS

This section presents the results of an exhaustive analysis using multiscale AM-FM for the purposes of characterizing retinal structures and classifying different types of lesions. As we have discussed in the previous section, the various retinal structures are encoded differently by the AM-FM features. Furthermore, we use frequency scales and filter banks to focus on the various size structures and eliminate noise introduced by other less meaningful structures that are present in the image.

Using the methodology previously described, the Mahalanobis distance values between features for each of the three estimates (IA, |IF|, and relative angle) and the nine CoS (Table II) are found. Tables IV and V show the maximum distance values and the corresponding estimate and combination found per lesion pair. For example, the maximum distance between hemorrhages and MAs is 4.71 standard deviations, and is given by the IA combination of scales #2 (IA-2 in Table V). Distances among the features range from 2.65 to 8.18 standard deviations, meaning that if we would use just this distance to classify the images, we would have accuracies between 92% and > 99.99%.

Most structures have their largest Mahalanobis distance from RB when using the |IF| features. Regions composed of only RB will have a histogram in most scales that reflects its high-frequency, random pixel brightness structure. Because vessels and the NV appear to have a predominant orientation in the IF, the relative IF angle can be used for differentiating vessels from MAs [see Fig. 9(b)], exudates, and hemorrhages. It can also be

TABLE V  
COMBINATION OF SCALES (SEE TABLE II) FOR THE  
MAXIMUM DISTANCES BETWEEN LESIONS

Retinal Structure	RB	EX	MA	HE	NV
EX	IF  - 7	-	-	-	-
MA	IF  - 6	IA - 9	-	-	-
HE	IF  - 2	IA - 1	IA - 2	-	-
NV	IA - 1	IA - 1	IA - 5	IA - 1	-
VE	IF  - 2	θ - 1	θ - 1	θ - 1	IF  - 1

seen that when only NV and vessels are used for discrimination purposes, the |IF| features are the most appropriate. This happens since the IA content may reflect similar information while the NV frequency components will vary significantly from components associated with a normal vessel. The regions with NV could also be differentiated using the angle estimation. This is the case for the classification between NV and hemorrhages [see Fig. 12(b)].

For differentiating between NV versus RB and MAs, the IA works best. From the results shown in Table IV, we see that the lowest Mahalanobis is between NV and HE. The distance obtained in our analysis is of 2.65 standard deviations. However, the distance between NV and RB is 8.18. From a clinical perspective, it is critically important to be able to isolate regions in the retina presenting with the high risk lesions, such as NV. Our results imply that NV will be classified or differentiated from the RB with greater than 99.99% accuracy and in the worst case with 92% of accuracy (NV versus HE).

Clinically significant macular edema (CSME) appears in an advanced stage of DR. This disease is characterized by exudates that appear near to the fovea. These were shown in Table IV to be easily differentiated from regions of RB ( $d = 6.87$ ) using the |IF| with CoS = 7. None of the other structures studied gave distances that are less than  $d = 3.31$ . IA provides the greatest distances to other structures except for the distance from exudates to RB. It can be observed that the maximum distance between exudates and MAs are obtained using the IA's extracted from medium and high frequencies. This occurs since the MAs have a smaller size than the exudates, and are thus characterized by higher frequencies.

For vessels, the relative angle and the |IF| provide relevant features for the discrimination of vessels from the rest of structures. The lower, medium, and higher frequencies are all involved in this characterization. This range of frequencies varies depending on the size of the element to which the vessels are compared. It is important to mention that in many MA segmentation studies, algorithms are often confounded by normal vessels segments and hemorrhages. For that reason, it is not surprising that although MAs are easily differentiated from RB ( $d = 3.48$ ), they are found to be similar, as measured by the Mahalanobis distance, to NV and normal retinal vessels ( $d = 2.83$  and  $d = 2.92$ , respectively).

Using the results shown in Tables IV and V, we can determine which CoS and which estimate provided the most relevant features for a particular comparison. These results are of great importance for our AM-FM algorithm since they allow us to pinpoint which are the features and CoS needed to separate

TABLE VI  
RELEVANT SCALES OF THE AM-FM ESTIMATES USING K-S TEST

Pair of Structures	Instantaneous Amplitude Scales	Instantaneous Frequency Magnitude Scales	Relative Angle Scales
RB, EX	1,3,4,5,6,7	1,3,4,5,6,7	5
RB, MA	4,6,7,	4,6,7	
RB, HE	2,3,4,6,7	3,4,6,7	2
RB, NV	1,3,4,5,6,7	1,4,5,6,7	
RB, VE	1,4,6,7	1,4,6,7	1,7
EX, MA	1,4,5,6,7	5,9	5
EX, HE	1,2,3,4,5,6,7	4,5,6	2
EX, NV	1,4,6,7	4,6	
EX, VE	1,2,4,5,6,7,8,9	2,7	2
MA, HE	1,2,4,6,7	2	2
MA, NV	1,4,5,6,7	1,7,9	
MA, VE	1,2,4,6,7	1,2,4,6	1,7
HE, NV	1,3,4,5,6,7,9	1,3,4,5,7,9	3
HE, VE	1,4,6,7	4,6	
NV, VE	1,3,4,5,6,7,8,9	1,2,4,6,7	

RB: Retinal Background, EX: Exudate  
MA: Microaneurysm, HE: Hemorrhage  
NV: Neovascularization, VE: Vessel

TABLE VII  
PERCENTILES OF THE DISTRIBUTIONS FOR EACH STRUCTURE

Retinal Structures	Retinal Background			Exudates			Microaneurysms		
	25	50	75	25	50	75	25	50	75
IA CoS 2	169.30	172.38	175.30	145.95	163.28	182.77	162.69	169.07	174.11
IA CoS 4	2.47	3.19	4.08	6.84	10.97	16.10	3.15	4.56	7.28
IA CoS 5	2.03	2.58	3.21	3.19	4.55	6.23	2.16	2.79	3.59
IF  CoS 2 (cycles/mm)	0.03	0.56	0.93	0.12	1.29	2.22	0.11	0.93	1.53

TABLE VIII  
PERCENTILES OF THE DISTRIBUTIONS FOR EACH STRUCTURE

Retinal Structures	Hemorrhages			Neovascularization			Vessels		
	25	50	75	25	50	75	25	50	75
IA CoS 2	99.64	110.81	120.92	126.98	134.59	141.91	123.53	142.29	153.17
IA CoS 4	3.33	4.65	6.27	5.89	8.13	10.80	3.66	6.48	12.83
IA CoS 5	2.32	2.96	3.72	3.03	4.05	5.26	2.37	3.23	4.37
IF  CoS 2 (cycles/mm)	0.07	1.04	1.71	0.04	1.07	1.81	0.15	1.42	2.23

the retinal structures. Knowing the relevant CoS, this step will reduce the numbers of features to be extracted. In addition to the Mahalanobis results that presents meaningful distance between CDFs of structures for all the CoS, the Kolmogorov--Smirnov test (KS-test) demonstrated that almost all the CoS and estimates provide useful information for the characterization of structures. Table VI shows that all CoS (from 1 to 9) between the three estimates are specified as relevant information for the classification. It can also be observed that the pair of structures in which the vessels are presented except vessels versus NV, the angle estimation helps in the discrimination of structures.

Finally, Table VIII presents a statistical analysis in percentiles for the most relevant estimates. It can be observed that, for the

IA-CoS 2, the hemorrhage presents values that are different from the rest of structures. This CoS is adequate for large structures ( $>0.226$  mm) since the lower frequencies are supported by it. Using the medium frequencies (CoS 5), we note that exudates and NV are clearly distinguished from the RB, while the MAs present similar values than the RB. This occurs since the medium frequencies capture structures comparable to exudates, the width of the NV, and the smallest structures such MAs, which are calls captured in high frequencies.

The following figures show the comparison of the mean of the CDFs between some of the pairs of structures from the list presented in Tables IV and V. The selected pairs include structures for which the majority of classification algorithms have

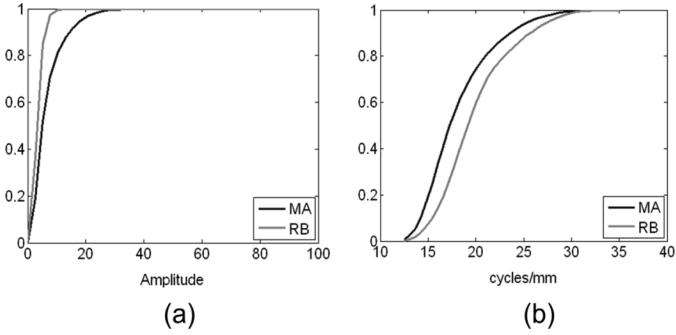


Fig. 8. Comparison of the mean of the CDFs between MA and RB. (a) CDFs of the IA for low and very low frequencies. (b) CDFs of the  $|IF|$  for low and very low frequencies.

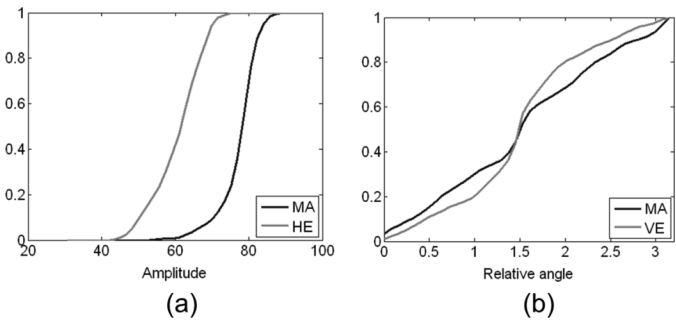


Fig. 9. (a) Comparison of the mean of the IA CDFs between MA and hemorrhage (HE) for the low-pass filter. (b) Comparison of the mean of the angle CDFs between MA and vessels (VE) for medium, low, and very low frequencies.

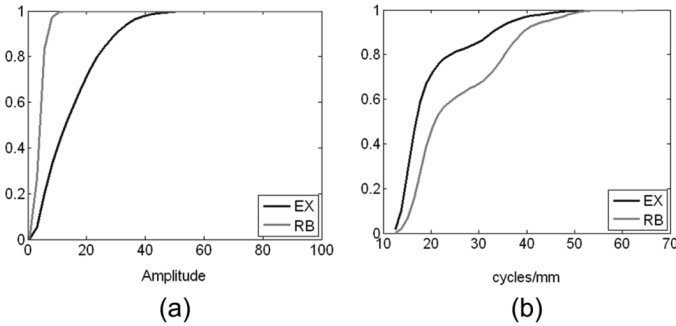


Fig. 10. Comparison of the mean of the CDFs between exudates (EX) and RB. (a) CDFs of the IA for medium and low frequencies. (b) CDFs of the  $|IF|$  for medium and low frequencies.

problems distinguishing between them. In Figs. 11 and 12, NV samples are compared with three different types of structures. This multiple comparison is presented due to the importance of NV, indicative of an advanced stage of DR. The common problem in the detection of the NV is that this type of lesion may have visually similar structures to hemorrhages and vessels, and therefore, similar analytical features that have previously produced inaccurate results using other image processing methods. In Fig. 12, the NV is compared with a hemorrhage using two different AM-FM estimates.

The characteristics of the AM-FM feature vectors that produced the distance table were shown in Figs. 8–12.

1) *Microaneurysms*: Fig. 8 compares MAs and RB using  $|IF|$  and IA for the combined L + VL frequency bands. The ROI that

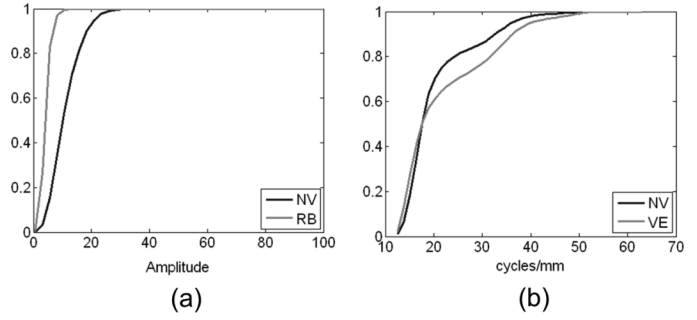


Fig. 11. (a) Comparison of the mean of the IA CDFs between NV and RB for medium, low, and very low frequencies. (b) Comparison of the mean of the  $|IF|$  CDFs between NV and vessels (VE) for medium, low, and very low frequencies.

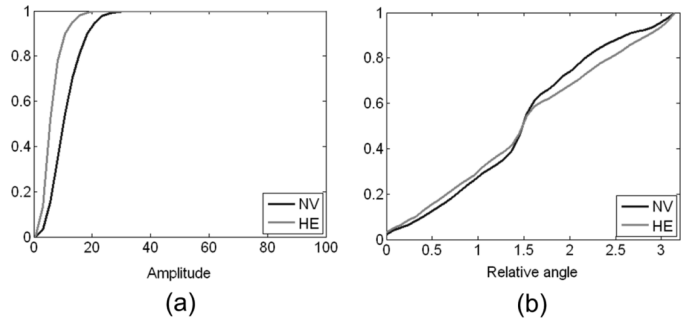


Fig. 12. Comparison of the mean of the CDFs between NV and Hemorrhage (HE). (a) CDFs of the IA for medium, low and very low frequencies. (b) CDFs of the  $\theta$  for low frequencies.

contains the MA displays a distribution of the  $|IF|$  that is shifted to the smaller magnitudes with respect to those of the RB for the low (L) and very low (VL) frequency bands [see Fig. 8(b)]. The RB, because of its near homogeneous gray level, presents a CDF for IA that rises sharply to 1, while the ROI with the MA will have a slower rise in the CDF or a broader distribution of the IA histogram [see Fig. 7(b)]. These differences are quantified in Table IV, where a Mahalanobis distance of 3.48 is observed.

Fig. 9 presents the CDFs for ROIs with MAs and hemorrhages [see Fig. 9(a)], and for MAs and retinal vessels [9(b)]. To differentiate MAs from hemorrhages IA from the lowest (LPF) frequency band gave the greatest Mahalanobis distance. This comes from the fact that hemorrhages exhibit strong low-frequency components due to their larger size. In comparison, ROIs with an MA were characterized by weaker low-frequency components, as seen by the faster rise in the IA CDF for MAs. MAs and retinal vessels are easily differentiated by the CDF of the relative IF angle. While MA angles are more evenly distributed, the retinal vessels clearly show a dominant orientation, as seen by the sharp rise at the central bin ( $\sim 20$ ) in the CDF for retinal vessels in Fig. 9(b).

2) *Exudates*: The maximum Mahalanobis distance for differentiating exudates from the RB (6.87 standard deviations) was given by the  $|IF|$  for medium (M) and low (L) frequency bands. This large distance between the two groups occurs mainly due to the fact that the RB is characterized by weaker medium and lower frequency content, while exudates have stronger components due to their well-defined size characteristics. Fig. 10 presents the CDFs for  $|IF|$  and IA. As with the MAs, detecting

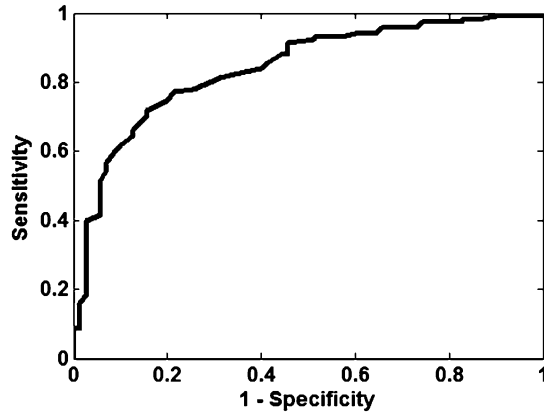


Fig. 13. ROC curve for the classification of: Risks 3, 2, and 1 versus Risk 0. Area under the ROC = 0.84. A best sensitivity/specificity of 92%/54% was obtained.

ROIs with exudates is facilitated by the broader distribution of the IA histogram as compared to the histograms for the RB.

3) *Neovascularization*: In Fig. 11(a) and (b) and Fig. 12(a) and (b), the NV is compared with the CDF for RB, retinal vessels, and hemorrhages, respectively. Table III shows Mahalanobis distances between neovascular abnormalities and RB, retina vessels, MAs, and hemorrhages as 8.18, 6.14, 2.92, and 2.65 standard deviations, respectively. This indicates a high probability of differentiation between NV and these other structures. The identifiable CDF of the ROIs with only RB is easily differentiated from ROIs with neovascular abnormalities through the IA CDF [see Fig. 11(a)] for the M + L + VL frequency band. |IF| was used to differentiate NV from normal retinal vessels. Fig. 11(b) shows the CDFs for the two types of structures using the M + L + VL frequency bands.

In Fig. 12(a) and (b), IA and |IF| are presented to illustrate that it is IA that gives the greatest contribution to the Mahalanobis distance between these two types of structures.

4) *Hemorrhages*: Large structures like hemorrhages have their stronger AM-FM components in the lower frequencies. For this reason, CoS with low frequencies are necessary to detect this kind of structure. Fig. 9(a) shows the comparison of the CDFs of the hemorrhages versus the MAs. It can be appreciated in the figure that the difference between both structures is large. On the other hand, when we use scales with that incorporate higher frequencies, the content of the hemorrhages cannot be detected completely. Fig. 12(a) shows the comparison of the hemorrhage versus NV for CoS 1. From this figure, it is clear that the IA for the hemorrhage is concentrated near zero, implying weaker components for the hemorrhages, as opposed to NV that has stronger components in the medium and higher frequencies.

5) *Vessels*: This structure can be differentiated using relative-angle estimates because it presents a well-defined geometrical orientation. Fig. 9(b) is a clear example of the expected shape for the vessels in which the CDF rises sharply at the center, as explained earlier.

As it can be seen in these plots of the CDF's, strong differences can be seen between different structures. To assess the significance of these features for the classification, the K-S test

TABLE IX  
DISTRIBUTION OF TRAINING AND TESTING DATA

DR Level	Training	Testing
Risk 0	70	70
Risk 1	18	9
Risk 2	30	39
Risk 3	70	70

TABLE X  
ABNORMAL IMAGES CORRECTLY CLASSIFIED PER RISK LEVEL

Level	Number	Percentage
Risk 3	70	97%
Risk 2	18	82%
Risk 1	30	89%
Total	108	92%

was applied for each pair of structures. In this analysis, each bin of the CDF of the structures is extracted. Since there are 20 regions per structure, each bin has a distribution with 20 elements. In this way, a meticulous analysis is performed to assess the relevance of the bins in our feature vector. Table VI shows the combination of scales that produced a significant difference between the structures pairs when using the K-S test. It can be observed that most of the CoS of the three estimates, specially the IA, contributed relevant information in the characterization of the DR lesions.

In addition to the previous analysis, the statistics for the distribution of the most relevant features for the classification are presented in Tables VII and VIII. These statistics were calculated with the pixel information for each of the 120 regions in our analysis. Tables VII and VIII present the median, and the 25 and 75 percentiles are presented for each of the six structures described before. These three quartiles are used to compare the population of all the CDFs for each structure.

Finally, automatic classification of DR and non-DR subjects was performed using the AM-FM features. Two experiments were conducted to determine the ability to correctly detect those images with signs of DR (see Table III). The first experiment consists of the classification of non-DR images versus DR images. We select half of our database for training purposes and the other half for testing purposes. Fig. 13 shows our ROC curve with an area of 0.84 with best sensitivity/specificity of 92%/54%. Table IX shows the distribution of images used in the training and testing sets, and Table X shows the percentage of images correctly classified using the best sensitivity/specificity

In addition to the previous experiment, a second experiment was performed. In this experiment, we took in account that diabetic patients with advanced forms of DR, such as clinical significant macular edema need to be referred immediately to an ophthalmologist for treatment. The Risk 3 and Risk 2 were further stratified into those with signs of CSME. Exudates within 1/3 disc diameter of the fovea was used as a surrogate for CSME. Table XI shows the distribution of images of the experiment IR versus normal images used for testing and training purposes. Since the number of images was smaller, the experiment was

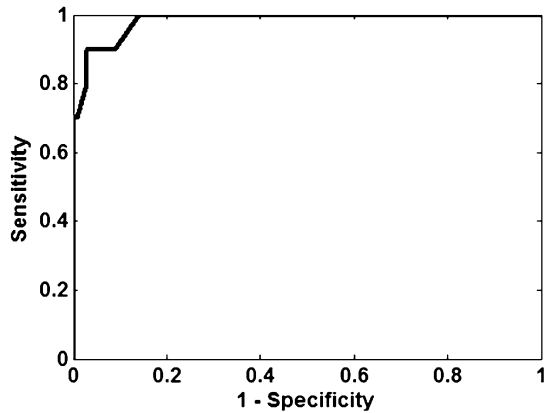


Fig. 14. ROC curve for the classification of the third experiment: IR versus Risk 0. A best sensitivity/specificity of 100%/88% was obtained.

TABLE XI  
DISTRIBUTION OF TRAINING AND TESTING DATA FOR THE IR EXPERIMENT

DR Level	Training	Testing
Risk 0	70	70
IR	18	9
Total	30	39

run 20 times with randomly selection of images, and the average result of  $AUC = 0.98$  is shown in Fig. 14.

#### IV. DISCUSSION AND CONCLUSION

The effectiveness of computer-based DR screening has been reported by several investigators, including an early commercial system, Retinalyze, by Larsen *et al.* [1]. Retinalyze produced a sensitivity of 0.97, a specificity of 0.71, and an AROC of 0.90 for 100 cases where two fields from two eyes (400 images total) were combined for identifying patients with DR. The specificity of the combined red and bright lesion detection could be improved to 78% by sorting and using only visually gradable quality images. The test data were from digitized 35 mm color slides and collected through dilated eyes.

More recently, Abràmoff *et al.* [30] achieved a sensitivity of 84% and specificity of 64% (0.84 area under the ROC). His retinal images were collected nonmydriatically and with variable compression of up to 100:1. The quality of this database is more representative of a screening environment, i.e., is dramatically worse than the samples provided by Larsen *et al.*, thereby suggesting a much more robust algorithm.

Abràmoff *et al.* results are consistent with the work of Fleming *et al.* [11], Lee *et al.* [31], and Sanchez *et al.* [32], who described a system in Aberdeen, Scotland *et al.* [33], where they reported a sensitivity of 90.5% and specificity of 67.4%, superior to manual reading of the same images. Our results compare well with the published results of these and others not mentioned.

Our algorithm demonstrated that the most advanced stage of DR (Risk 3) was strongly differentiated from the non-DR (Risk 0) images, assuring that most of the lesions in the retina could be captured using the features provided by AM-FM. The classification using the features extracted with AM-FM demonstrated

an efficient methodology to detect DR. Using the AM-FM technique to extract the features, good sensitivity for the abnormal images versus abnormal images and high sensitivity/specificity for IR versus normal images were obtained.

This algorithm allows the user to obtain a detailed analysis of the images since the features are extracted by regions. Then a combination of unsupervised and supervised methods are used for global classification. In this way, all lesion kinds could be detected without the need of manually segmentation by a technician.

This paper reports on the first time that AM-FM has been used with a multiscale decomposition of retinal structures for the purposes of classifying them into pathological and normal structures. The results demonstrate a significant capability to differentiate between retinal features, such as normal anatomy (RB and retinal vessels), from pathological structures (NV, MAs, hemorrhages, and exudates). The histograms for ROI containing these structures yield a signature through the CDF that can be used to successfully differentiate these structures as summarized in Table VI.

The application of the proposed methodology to DR screening is new. The principal advantage of this approach is that the methodology can be trained with only global classification of images, e.g., no DR or DR present, without having to develop a training database that requires each lesion to be annotated. CDFs for an image classified as having no DR can be used to establish a normative database. Deviations from this normative database will reflect potential pathological ROIs, and the image and ROI can be marked as such. This capability will allow rapid retraining, if necessary, on any database of retinal images with different spatial resolution, field of view, image compression, etc. This is an important capability where a large number of imaging protocols are used with a variety of digital cameras.

#### ACKNOWLEDGMENT

The authors would like to thank Méthodes d'Evaluation de Systèmes de Segmentation et d'Indexation Dédicées à l'Ophtalmologie Rétinienne for allowing them to use their database in this study.

#### REFERENCES

- [1] M. Larsen *et al.*, "Automated detection of fundus photographic red lesions in diabetic retinopathy," *Invest. Ophthalmol. Vis. Sci.*, vol. 44, pp. 761–766, 2003.
- [2] M. Niemeijer, S. R. Russell, M. A. Suttorp, B. van Ginneken, and M. D. Abràmoff, "Automated detection and differentiation of drusen, exudates, and cotton-wool spots in digital color fundus photographs for early diagnosis of diabetic retinopathy," *Invest. Ophthalmol. Vis. Sci.*, vol. 48, pp. 2260–2267, 2007.
- [3] M. Niemeijer, B. van Ginneken, J. Staal, M. S. A. Suttorp-Schulten, and M. D. Abràmoff, "Automatic detection of red lesions in digital color fundus photographs," *IEEE Trans. Med. Imag.*, vol. 24, no. 5, pp. 584–592, May 2005.
- [4] B. Sander *et al.*, "Automatic detection of fundus photographic red lesions in diabetic retinopathy," presented at the Assoc. Res. Vis. Ophthalmol. Conf., Fort Lauderdale, FL, 2001, Poster 4338.
- [5] V. Murray, "AM-FM methods for image and video processing." Ph.D. dissertation, Univ. New Mexico, Albuquerque, Sep. 2008.
- [6] A. Osareh, M. Mirmehdi, B. Thomas, and R. Markham, "Automated identification of diabetic retinal exudates in digital colour images," *Br. J. Ophthalmol.*, vol. 87, pp. 1220–1223, 2003.

- [7] A. Osareh, M. Mirmehdi, B. Thomas, and R. Markham, "Classification and localisation of diabetic-related eye disease," in *Proc. 7th Eur. Conf. Comput. Vis.*, 2002, pp. 325–329.
- [8] T. Spencer, J. A. Olson, K. C. McHardy, P. F. Sharp, and J. V. Forrester, "An image-processing strategy for the segmentation and quantification of microaneurysms in fluorescein angiograms of the ocular fundus," *Comput. Biomed.*, vol. 29, pp. 284–302, 1996.
- [9] A. Frame *et al.*, "A comparison of computer based classification methods applied to the detection of microaneurysms in ophthalmic fluorescein angiograms," *Comput. Biol. Med.*, vol. 28, pp. 225–238, 1998.
- [10] M. Niemeijer, B. van Ginneken, J. Staal, M. S. A. Suttorp-Schulten, and M. D. Abràmoff, "Automatic detection of red lesions in digital color fundus photographs," *IEEE Trans. Med. Imag.*, vol. 24, no. 5, pp. 584–592, May 2005.
- [11] A. D. Fleming, S. Philip, K. A. Goatman, G. J. Williams, J. A. Olson, and P. F. Sharp, "Automated detection of exudates for diabetic retinopathy screening," *Phys. Med. Biol.*, vol. 52, pp. 7385–7396, 2007.
- [12] E. Ricci and R. Perfetti, "Retinal blood vessel segmentation using line operators and support vector classification," *IEEE Trans. Med. Imag.*, vol. 26, no. 10, pp. 1357–1365, Oct. 2007.
- [13] J. Staal, M. D. Abràmoff, M. Niemeijer, M. A. Viergever, and B. van Ginneken, "Ridge based vessel segmentation in color images of the retina," *IEEE Trans. Med. Imag.*, vol. 23, no. 4, pp. 501–509, Apr. 2004.
- [14] J. G. Leandro, R. M. Cesar, and H. Jelinek, "Blood vessels segmentation in retina: Preliminary assessment of the mathematical morphology and of the wavelet transform techniques," in *Proc. 14th Brazilian Symp. Comput. Graph. Image Process., SIBGRAPI IEEE Comput. Soc.*, 2001, pp. 84–90.
- [15] M. Niemeijer, S. R. Russell, M. A. Suttorp, B. Van Ginneken, and M. D. Abràmoff, "Automated detection and differentiation of drusen, exudates, and cotton-wool spots in digital color fundus photographs for early diagnosis of diabetic retinopathy," *Invest. Ophthalmol. Vis. Sci.*, vol. 48, pp. 2260–2267, 2007.
- [16] L. Streeter and M. Cree, "Microaneurysm detection in colour fundus images," *Image Vis. Comput.*, pp. 280–285, 2003.
- [17] H. J. Jelinek, M. J. Cree, D. Worsley, A. Luckie, and P. Nixon, "An automated microaneurysm detector as a tool for identification of diabetic retinopathy in rural optometric practice," *Clin. Exp. Optom.*, vol. 89, pp. 299–305, 2006.
- [18] A. Sopharak and B. Uyyanonvara, "Automatic exudates detection from diabetic retinopathy retinal image using fuzzy c-means and morphological methods," in *Proc. 3rd IASTED Int. Conf. Adv. Comput. Sci. Technol.*, Phuket, Thailand, 2007, pp. 359–364.
- [19] T. Walter, J. C. Klein, P. Massin, and A. Erginay, "A contribution of image processing to the diagnosis of diabetic retinopathy-detection of exudates in colour fundus images of the human retina," *IEEE Trans. Med. Imag.*, vol. 21, no. 10, pp. 1236–1243, Oct. 2002.
- [20] D. Vallabha, R. Dorairaj, K. Namuduri, and H. Thompson, "Automated detection and classification of vascular abnormalities in diabetic retinopathy," presented at the Asilomar Conf. Signals, Syst. Comput., Pacific Grove, CA, 2004.
- [21] G. Quéllec, M. Lamard, P. Josselin, and G. Cazuguel, "Optimal wavelet transform for the detection of microaneurysm in retina photographs," *IEEE Trans. Med. Imag.*, vol. 27, no. 9, pp. 1230–1241, Sep. 2008.
- [22] G. Quéllec, M. Lamard, P. Josselin, G. Cazuguel, B. Cochener, and C. Roux, "Detection of lesions in retina photographs based on the wavelet transform," in *Proc. 28th IEEE EMBS Annu. Int. Conf.*, 2006, pp. 2618–2621.
- [23] M. Sofka and C. V. Stewart, "Retinal vessel extraction using multi-scale matched filters confidence and edge measures," *IEEE Trans. Med. Imag.*, vol. 25, no. 12, pp. 1531–1546, Dec. 2005.
- [24] M. Al-Rawi, M. Qutaishat, and M. Arrar, "An improved matched filter for blood vessel detection of digital retinal images," *Comput. Biol. Med.*, vol. 37, no. 2, pp. 262–267, 2007.
- [25] Fundus Photograph Reading Center Dept. Ophthalmol. Vis. Sci., Univ. Wisconsin, Madison [Online]. Available: <http://eyephoto.ophth.wisc.edu/ResearchAreas/Diabetes/DiabStds.htm>
- [26] M. S. Pattichis and A. C. Bovik, "Analyzing image structure by multi-dimensional frequency modulation," *IEEE Trans. Pattern Anal. Mach. Intell.*, vol. 29, no. 5, pp. 753–766, May 2007.
- [27] J. P. Havlicek, "AM-FM image models," Ph.D. dissertation, Univ. Texas at Austin, Austin, 1996.
- [28] V. Murray, P. Rodriguez, and M. S. Pattichis, "Multi-scale AM-FM demodulation and reconstruction methods with improved accuracy," *IEEE Trans. Image Process.*, to be published.
- [29] MESSIDOR: Methods to evaluate segmentation and indexing techniques in the field of retinal ophthalmology TECHNO-VISION Project [Online]. Available: <http://messidor.crihan.fr/>
- [30] M. D. Abràmoff, N. Meindert, M. A. Suttorp-Schulten, M. A. Viergever, S. R. Russell, and B. van Ginneken, "Evaluation of a system for automatic detection of diabetic retinopathy from color fundus photographs in a large population of patients with diabetes," *Diabetes Care*, vol. 31, pp. 193–198, 2008.
- [31] S. C. E. T. Lee, Y. Wang, R. Klein, R. M. Kingsley, and A. Warn, "Computer classification of non-proliferative diabetic retinopathy," *Arch. Ophthalmol.*, vol. 123, pp. 759–764, 2005.
- [32] C. I. Sánchez, R. Hornero, M. I. López, and J. Poza, "Retinal image analysis to detect and quantify lesions associated with diabetic retinopathy," in *Proc. Int. Conf. IEEE Eng. Med. Biol. Soc.*, 2004, vol. 3, pp. 1624–1627.
- [33] S. Philip, A. D. Fleming, K. A. Goatman, S. Fonseca, P. Mcnamee, G. S. Scotland, G. J. Prescott, P. F. Sharp, and J. A. Olson, "The efficacy of automated "disease/no disease" grading for diabetic retinopathy in a systematic screening programme," *Br. J. Ophthalmol.*, vol. 91, pp. 1512–1517, 2007.